nature chemistry

ARTICLES

PUBLISHED ONLINE: 4 SEPTEMBER 2011 | DOI: 10.1038/NCHEM.1140

Efficient water oxidation catalysts based on readily available iron coordination complexes

Julio Lloret Fillol*, Zoel Codolà, Isaac Garcia-Bosch, Laura Gómez, Juan José Pla and Miquel Costas*

Water oxidation catalysis constitutes the bottleneck for the development of energy-conversion schemes based on sunlight. To date, state-of-the-art homogeneous water oxidation catalysis is performed efficiently with expensive, toxic and earth-scarce transition metals, but 3*d* metal-based catalysts are much less established. Here we show that readily available, environmentally benign iron coordination complexes catalyse homogeneous water oxidation to give O_2, with high efficiency during a period of hours. Turnover numbers >350 and >1,000 were obtained using cerium ammonium nitrate at pH 1 and sodium periodate at pH 2, respectively. Spectroscopic monitoring of the catalytic reactions, in combination with kinetic studies, show that high valent oxo-iron species are responsible for the O–O forming event. A systematic study of iron complexes that contain a broad family of neutral tetradentate organic ligands identifies first-principle structural features to sustain water oxidation catalysis. Iron-based catalysts described herein open a novel strategy that could eventually enable sustainable artificial photosynthetic schemes.

Replacing petroleum by an energy system that uses sustainable fuel and reduces CO_2 emissions is among the most critical issues of today's society. Although energy consumption per year is predicted to increase from 529 EJ in 2010 to 780 EJ by 2035, the natural supplies of petroleum are diminishing[1–3]. At the same time, CO_2 emissions are widely considered as the main factor that contributes to climate change. In this context, the use of hydrogen as an optimal energy carrier holds high potential. Its water–solar production is envisioned as one of the most promising approaches with regard to sustainability and energy security, and also to avoid undesirable emissions. However, fundamental technological challenges remain unsolved[4,5]: water splitting into H_2 and O_2 is a multielectron process coupled with a multiple-proton transference in an uphill energy transformation (equation (1)). In this regard, the multielectron transference is underlined as a general chemical problem[6].

$$2H_2O \xrightarrow{h\nu} 2H_2 + O_2 \quad \Delta G^0 = 4.92\ \text{eV}\ (113\ \text{kcal mol}^{-1}) \tag{1}$$

$$4H^+ + 4e^- \longrightarrow 2H_2 \tag{2}$$

$$2H_2O \longrightarrow O_2 + 4H^+ + 4e^- \tag{3}$$

Water splitting consists of two processes, H_2 formation and water oxidation (equations (2) and (3)). Equation (3) is identified as the bottleneck because it requires a multielectron stepwise building up of very high redox potentials. Despite these enormous chemical challenges, water oxidation is essential because the reaction produces O_2, and water is the only waste-free electron-source substrate that could sustain the scale (multibillion tonnes) of the process required to supply our energy demands. Water oxidation takes place at the oxygen-evolving complex of photosystem II (PSII) in green plants, and constitutes one of the basic elements of photosynthesis, the process by which sunlight energy is employed to reduce CO_2 and form carbohydrates[7]. As a result of its technological relevance, currently major research efforts are devoted to the development of artificial photosystems and heterogeneous photocatalytic materials[8,9]. Seminal studies on earth-scarce ruthenium[10] and, more recently, iridium[11–13] metals, both combined with organic ligand frameworks, led to the discovery of highly effective artificial molecular catalytic systems that operate under homogeneous conditions (≈10,000 turnover number (TON), the number of O_2 molecules produced/the number of catalyst molecules used). However, the limited abundance of these metals in the earth's crust (≈1 parts per 10^9), their high price in the market and their toxicity restrict their use on a large scale. Thus we need to develop water oxidation catalysts (WOCs) based on the first-row transition metals (regarded as abundant, environmentally benign and inexpensive catalyst alternatives) and on iron in particular[14].

To date, few artificial WOCs that operate in homogeneous conditions and are based on first-row transition metals have been discovered[15–22]. These catalysts generally rely on very unique polyoxometallate (POM) frameworks or rather complex ligand architectures, and provide modest turnover/metal centre numbers (TON ≈ 78) (refs 20,21). The unique stability of POMs against oxidation makes them the most promising way to develop artificial photosystems that could operate over long periods of time. However, only a few examples of POMs based on first-row transition metals and capable of performing water oxidation catalysis are reported. In addition, attempts to introduce structural changes resulted in a loss of catalytic activity[20], which therefore prevented further improvement. For the specific case of well-defined iron-based catalysts, a single precedent was reported by the groups of Collins and Bernhard, who described that iron(III) complexes with tetraamido macrocyclic ligands (Fe-TAMLs) are fast WOCs[22]. However, the activity vanishes after a few seconds (TON = 16, turnover frequency (TOF = TON h^{-1}) maximum of 4,680 h^{-1}). Consequently, the discovery of efficient WOCs based on abundant, inexpensive and non-toxic metals that could be improved easily by using rational and simple synthetic schemes remains a challenge.

Towards this goal, herein we report a large family of catalytic systems based on iron and containing straightforward, accessible modular tetradentate nitrogen-based ligands, which are able to

Departament de Química, Universitat de Girona, Campus Montilivi, 17071 Girona, Spain. *e-mail: Julio.lloret@udg.edu; Miquel.costas@udg.edu

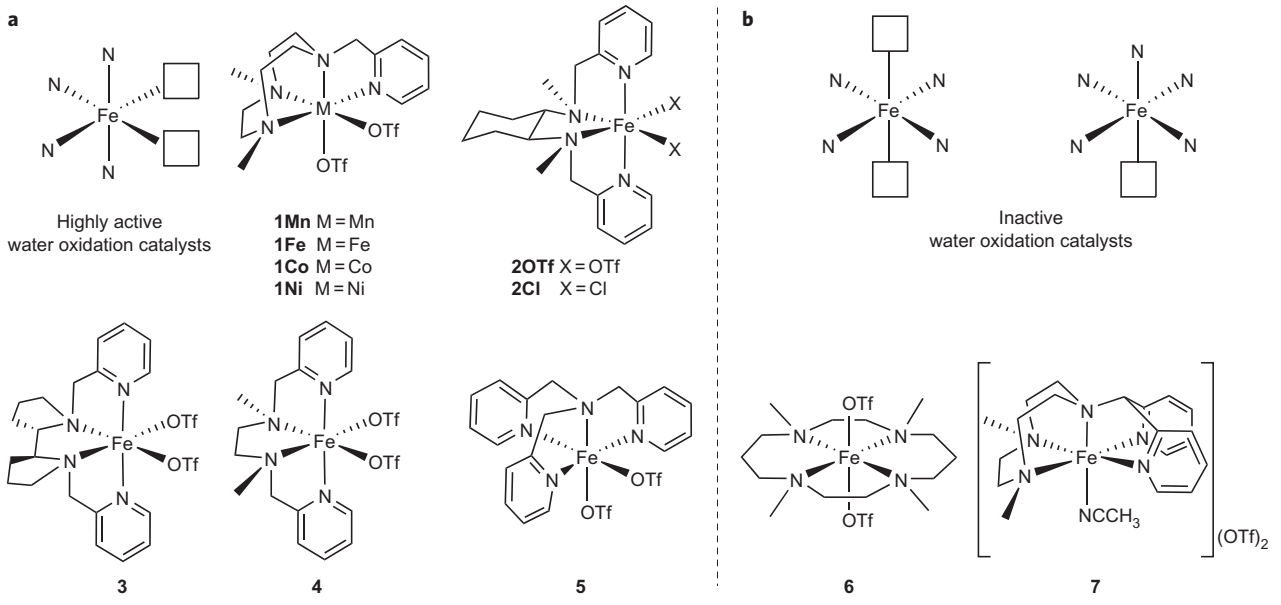

Figure 1 | Transition metal complexes used in this study. a, Complexes found to be active had neutral tetradentate nitrogen ligands that gave two *cis* free coordination sites. The most active catalyst is in the top left. **b**, In contrast, tetradentate nitrogen ligands that gave *trans* free coordination sites and pentadentate neutral nitrogen ligands were found to be inactive in water oxidation catalysis.

Table 1 | $[M(OTf)_2(^{Me2}Pytacn)]$ complexes and screening conditions for catalytic water oxidation.

Catalyst	[Catalyst] (μM)	Oxidant	[Oxidant] (mM)	TON*	TOF†
$[Mn(OTf)_2(^{Me2}Pytacn)]$, **1Mn**	37.5	CAN or $NaIO_4$	125	-	-
$[Co(OTf)_2(^{Me2}Pytacn)]$, **1Co**	37.5	CAN or $NaIO_4$	125	-	-
$[Ni(OTf)_2(^{Me2}Pytacn)]$, **1Ni**	37.5	CAN or $NaIO_4$	125	-	-
$[Fe(OTf)_2(^{Me2}Pytacn)]$, **1Fe**	37.5	CAN	125	70±5	436
$[Fe(OTf)_2(^{Me2}Pytacn)]$, **1Fe**	12.5	CAN	125	82±8	222
$[Fe(OTf)_2(mcp)]$, **2OTf**	12.5	CAN	125	360±20	838
$[FeCl_2(mcp)]$, **2Cl**	12.5	CAN	125	320±15	515
$[(Fe(mcp))_2(\mu\text{-}O)(\mu\text{-}OH)](OTf)_2$, **2μ-(O,OH)**‡	6.25	CAN	125	210±21	105
$[Fe(OTf)_2(mcp)]$, 2OTf	12.5	**$NaIO_4$**	**125**	**>1,050**	**222**
$[Fe(OTf)_2(bpbp)]$, **3**	12.5	CAN	125	63±7	167
$[Fe(OTf)_2(mep)]$, **4**	12.5	CAN	125	145±5	503
$[Fe(OTf)_2(tpa)]$, **5**	12.5	CAN	125	40±4	53
$[Fe(OTf)_2(tmc)]$, **6**	12.5	CAN or $NaIO_4$	125	-	-
$[Fe(NCCH_3)(^{Me}Py_2CH\text{-}tacn)](OTf)_2$, **7**	12.5	CAN or $NaIO_4$	125	-	-
$[Co_4(H_2O)_2(PW_9O_{34})_2]^{-10}$§		$[Ru(bpy)_3]^{3+}$	1.5	78	18,000
$Co(NO_3)_2$‖		$[Ru(bpy)_3]^{3+}$	1.5	23	-
Fe(III)-TAML¶		CAN	0.146	16	4,680

All the reactions were performed in water at room temperature (r.t.). *Maximum TON. †TOF under initial rate ($TON{\cdot}h^{-1}$). TON and TOF values were averaged over three reactions, with errors below 10%. ‡Concentration per metal = 12.5 μM. §Co complex (3.2 μmol), sodium phosphate buffer (30 mM), initial pH = 8.0, $[Ru(bpy)_3](ClO_4)_3$ (1.5 mM) and r.t. (ref. 20). ‖Co^{2+} complex (13.0 μmol), sodium phosphate buffer (30 mM), initial pH = 8.0, $[Ru(bpy)_3](ClO_4)_3$ (1.5 mM) and r.t. (ref. 20). ¶Catalyst (0.78 μmol) with cerium(IV) (145.7 μmol) in a total volume of 0.8 ml of non-buffered water[22].

perform the oxidation of water with high efficiency (Fig. 1). Preliminary mechanistic studies indicate the basic design principles that govern the catalytic activity and that may upgrade iron as the metal of choice for water oxidation catalysis.

Results and discussion

Initially, we focused our efforts on the chelating tetradentate ligand 1-(2′-pyridylmethyl)-4,7-dimethyl-1,4,7-triazacyclononane) (^{Me2}Pytacn) combined with the first-row redox-active transition metals cobalt, iron, manganese and nickel. The ligand was chosen because it sustains highly active oxidation catalysts and because of its capacity to stabilize high oxidation states[23–25]. The catalytic water-oxidation activity of a series of $[M(OTf)_2(^{Me2}Pytacn)]$ (M = Ni, Co, Fe, Mn, $OTf = CF_3SO_3^-$) complexes dissolved in water was tested using cerium(IV) ammonium nitrate (CAN) or sodium periodate ($NaIO_4$) as sacrificial oxidants (Table 1). Remarkably, water-soluble $[Fe(OTf)_2(^{Me2}Pytacn)]$ (**1Fe**) was found to be highly active, with gas bubbles observed after the addition of oxidant. The reaction of 1 mM of **1Fe** with 75 mM of CAN led to a total of 18 catalytic cycles with a TOF of 233. In contrast, all attempts to oxidize water with $[M(OTf)_2(^{Me2}Pytacn)]$ (M = Mn (**1Mn**), Co (**1Co**) and Ni (**1Ni**)) failed. Gas chromatography (GC) and mass spectrometry (MS) analysis of the gas obtained from the reaction confirmed the presence of dioxygen as the unique gaseous product. Furthermore, when the reaction was carried out under argon in degassed $H_2{}^{16}O$ or $H_2{}^{18}O$, only $^{16}O = {}^{16}O$ and $^{18}O = {}^{18}O$ were detected, respectively. Likewise, the O_2 isotopic distribution obtained when using a solvent mixture of $H_2{}^{16}O$:$H_2{}^{18}O$ 1:1 (v:v) was $^{16}O = {}^{16}O/{}^{16}O = {}^{18}O/{}^{18}O = {}^{18}O = 28/50/22$, respectively (Supplementary Fig. S2). Overall, these experiments demonstrate conclusively that O_2 originated from water oxidation.

Based on these promising results, we decided to study in detail the oxidation of water catalysed by **1Fe**. The most relevant data are summarized in Table 1 and in Supplementary Tables S1 and

S2. The system activity depends strongly on the concentration of both the catalyst (1–0.01 mM) and the oxidant (50–200 mM). The maximum activity for complex **1Fe** was observed at 12.5 μM of catalyst and 125 mM of CAN, rising up to 82±8 TON for 12.5 μM (at lower concentrations the activity increased, but because of our analytical systems we found lower reproducibility). Isotopic analysis experiments performed under catalytically relevant conditions (125 mM CAN, 40 μM **1Fe**) again showed that the isotopic content of the evolved O_2 matched the statistic distribution of the water solution (see Supplementary Information for details), which demonstrates that it is the product of the oxidation of water. It is known that metal-oxide nanoparticles can catalyse water oxidation. Therefore, we carried out dynamic light scattering (DLS) and nanoparticle-tracking analysis (NTA) studies to explore whether water-oxidation activity could be the result of nanoparticles formed *in situ* (see Supplementary Information for details). DLS and NTA analyses indicated that no significant formation of iron-oxide nanoparticles took place, which strongly suggests that the observed catalysis truly originated from the water-soluble iron molecular complex.

At this point we explored potential structural features of the iron complexes required for effective water oxidation. The very robust neutral tetradentate pyridine triazacyclononane ligand ^{Me2}Pytacn coordinates strongly through three aliphatic amines and one pyridine to the iron centre, leaving two adjacent extra coordination sites. In light of this, we studied some prototypical nitrogen-based ligands with diverse coordination, electronic and steric properties.

The closely related iron complexes **2Cl**, **2OTf**, **3**, **4** and **5** bearing tetradentate nitrogen ligands (*N*,*N*′-dimethyl-*N*,*N*′-bis(2-pyridylmethyl)-cyclohexane-1,2-diamine (mcp), *N*,*N*′-dimethyl-*N*,*N*′-bis-(2-pyridylmethyl)-ethane-1,2-diamine (mep), *N*,*N*′-bis(2-pyridylmethyl)-2,2′-bipyrrolidine (bpbp), tris-(2-pyridylmethyl)amine (tpa) (Fig. 1)) present two main modifications with respect to the ligand ^{Me2}Pytacn: lower coordination rigidity and lower ligand basicity. At the same time, this set of complexes shares a common tetradentate coordination arrangement that leaves two accessible coordination sites in *cis*-relative positions. Very remarkably, all the complexes were active under our standard catalytic conditions (iron complex, 12.5 μM; CAN, 125 mM), but clear differences among them were evident (Fig. 2 and Table 1). Complex **5** (TON, 40±4; TOF, 53 h^{-1}) was the least active of the series. Nonetheless, it is remarkably effective with respect to the single precedent reported with iron-based catalysts and CAN (16 TON for Fe-TAMLs)[22]. Complexes **2OTf** (TON, 360±20; TOF, 838 h^{-1}), **3** (TON, 63±7; TOF, 167 h^{-1}) and **4** (TON, 145±5; TOF, 503 h^{-1}) share a common structural topology and, interestingly, all of them present similar or higher activities and efficiencies than those of complex **1Fe**. Complex **4** was over twofold more active than **1**, but more interesting were the results yielded by complexes **2OTf** and **2Cl**, which gave the highest number of catalytic cycles per iron atom (**2OTf** yielded a TON of 360±20 and a TOF of 838 h^{-1}; **2Cl** yielded a TON of 320±15 and a TOF of 515 h^{-1}). This result indicates that weak coordinating anions, such as the trifluoromethanesulfonate, are not mandatory and the use of simple chloride anions yields comparable results. Time traces shown in Fig. 2 indicate that catalytic water-oxidation activity of the complexes stops after 1–3 hours, despite the large excess of oxidant still present. These observations are attributed to catalyst degradation under the strong oxidizing and acidic catalysis experimental conditions.

The iron(III) oxohydroxo diferric dimer **2μ-(O,OH)** showed a lower reaction rate and different kinetic behaviour, which discard the oxohydroxo dimeric structures as important active intermediates of the studied iron(II) complexes (Supplementary Fig. S9). Interestingly, complexes **6** and **7**, which have two *trans* and only one available coordination site, respectively, are inactive. This

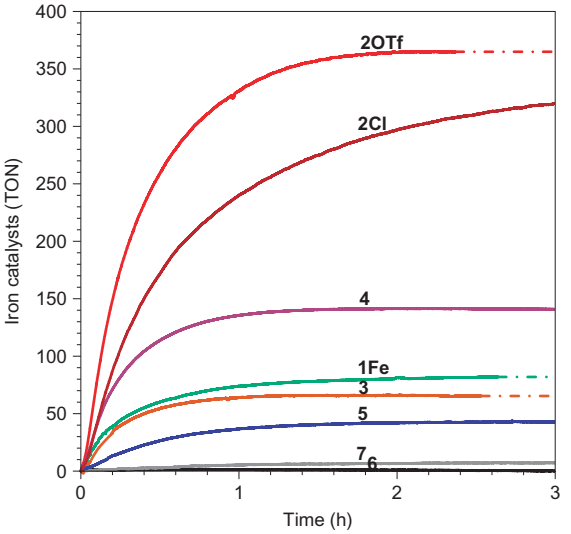

Figure 2 | TON versus time. On-line oxygen-evolution traces for the reactions of 12.5 μM of the iron catalysts with 125 mM of CAN. The most active complexes were **2OTf** (red) and **2Cl** (brown). The graph indicates that the nature of the anion has a remarkable effect, but nevertheless both complexes were highly active.

observation strongly suggests that the presence of *cis* labile sites is the key structural feature for eliciting water oxidation catalysis. Finally, we investigated $NaIO_4$ as an alternative oxidant for the most active complex **2**. Surprisingly, the number of catalytic cycles increased to more than 1,050 at an initial pH of 2, adjusted with triflic acid. Insight into the mechanism of O_2 formation in the reactions with $NaIO_4$ was obtained from isotopic labelling experiments. When an isotopic mixture of $H_2{}^{18}O$:$H_2{}^{16}O$ 6.5%:93.5% was used as solvent in the reaction of **2** with $NaIO_4$, analysis of the evolved O_2 by MS showed an isotopic pattern in excellent agreement with a statistical distribution of the isotopic water composition (see Supplementary Section S4 for details). This observation shows that O_2 originated from water oxidation and not by $NaIO_4$ decomposition. However, this conclusion should be treated with caution at long reaction times because $NaIO_4$ undergoes exchange of its oxygen atoms with water, as demonstrated by electrospray ionization mass spectroscopy (ESI-MS) time-course experiments (see Supplementary Information). As a result, the isotopic distribution of O_2 measured at long reaction times could not demonstrate unambiguously a water-oxidation origin. Nevertheless, we found no reason to believe that such a change in the mechanism of O_2 evolution occurs over time. Furthermore, O_2 evolution is observed only for those catalysts that perform water oxidation with CAN (Table 1). The sum of these experimental observations provides compelling evidence that O_2 is produced in these reactions only by water oxidation, and it is not formed from periodate decomposition.

To the best of our knowledge, the values of catalytic cycles per metal centre (>1,000) attained by these iron catalysts are the highest reported for any homogeneous system based on first-row transition metals. Furthermore, the chemical structures of these water-soluble catalysts can be modified easily in a systematic manner, and in this regard further optimization is envisioned.

Kinetic studies. Little is known about the resting states, oxidation states and nuclearity of WOCs based on first-row transition metals. To obtain some insight into our Fe-based systems, we studied the **1Fe** catalyst as a prototypical case for complexes of the general formula $[Fe(X)_2(L^{N4})]$, where L^{N4} stands for a tetraazadentate ligand and X is a Cl or OTf ligand in a relative *cis*-position. We first titrated a freshly prepared **1Fe** (1 mM) solution in water with

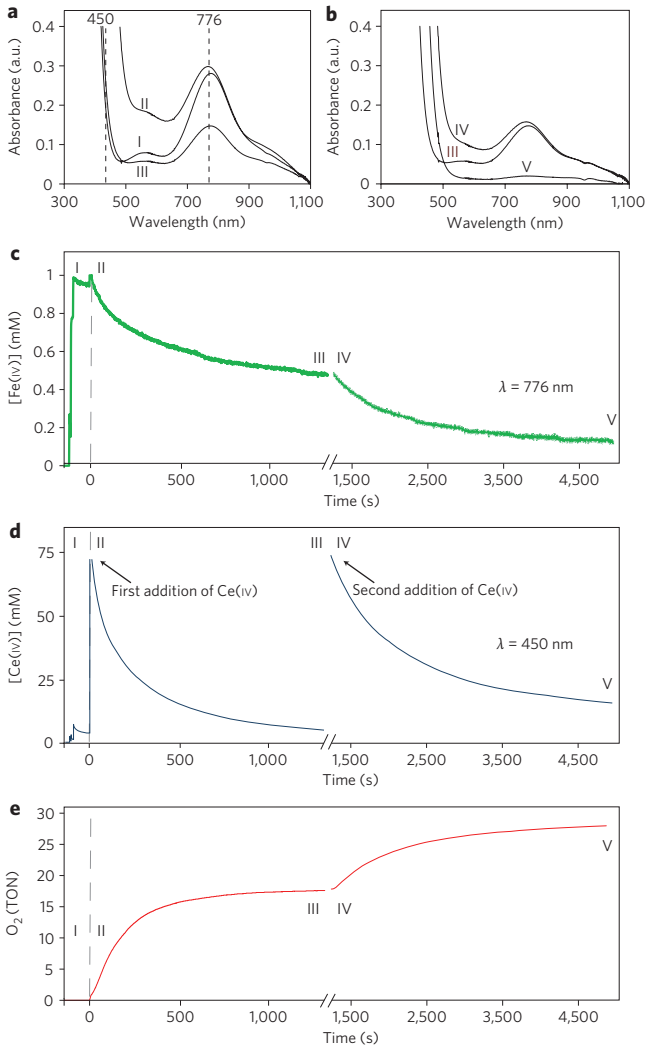

Figure 3 | Oxygen formation and cerium(IV) consumption monitored on-line by a pressure transducer and UV-vis spectrometry. a, UV-vis spectra of **1Fe(IV)=O** generated by reacting complex **1Fe** (1 mM) solution in water with 6 equiv. of Ce(IV) (I), on the addition of 75 equiv. of Ce(IV) to **1Fe(IV)=O** (II) and after all the Ce(IV) was consumed and no further oxygen evolution was observed (III). a.u. = arbitrary units. **b**, Spectrum recorded after a second addition of 75 equiv. of Ce(IV) (IV) and the final spectrum after all **1Fe(IV)=O** was consumed, and no more oxygen evolved (V). **c**–**e**, Kinetic traces of [**1Fe(IV)=O**] (mM) monitored at 776 nm (**c**), of [Ce(IV)] (mM) monitored at 450 nm (**d**) and of $\Delta[O_2]$ (TON) monitored by a pressure transducer (**e**).

Ce(IV). The addition of 6 equiv. of CAN to a solution of **1Fe** (1 mM) led to a new band at $\lambda_{max} = 776$ nm and $\varepsilon = 280\ M^{-1}\ cm^{-1}$ in the ultraviolet–visible (UV-vis) spectrum, characteristic of $[Fe(IV)(O)(H_2O)(^{Me2}Pytacn)]^{2+}$, **1Fe(IV)=O**, which appeared to be formed quantitatively on the basis of the intensity of the band (Fig. 3, spectrum I)[24]. Further characterization of **1Fe(IV)=O** was obtained by ESI-MS (Supplementary Fig. S4) in H_2O and matched that of the recently described **1Fe(IV)=O** recorded in acetonitrile[24]. Under these conditions, **1Fe(IV)=O** was persistent, with a half-life of 2.4 hours. This high stability clearly indicates that water oxidation does not take place at **1Fe(IV)=O**. On further addition of 75 equiv. of CAN the pressure transducer recorded a fast increase of the gas pressure up to 17.6 equiv. of oxygen. The oxygen evolution was in agreement with the cerium consumption (ratio $(Ce(IV)/O_2) = 4.2$; further information is given in Supplementary Fig. S11 and Table S3).

In parallel, the absorbance of the UV-vis spectral features that correspond to Ce(IV) and **1Fe(IV)=O** decreased (Fig. 3, spectrum II → spectrum III). When all the Ce(IV) was consumed the UV-vis spectrum showed that the concentration of **1Fe(IV)=O** had decreased by about 50% (Fig. 3, spectrum III). Further, 10.7 TON of O_2 was generated by a subsequent CAN (75 equiv.) addition with concomitant Ce(IV) and oxo-iron(IV) consumption. The initial TOF after the first CAN addition was 233 h^{-1}. The initial TOF after the second CAN addition was smaller (89 h^{-1}). The second TOF value could be estimated as 50% of the first value. The system is very complex and the slight change in TOF may have multiple reasons. For example, a physical change on the reaction medium, such as pH or the presence of Ce(III), could modify the reaction rate. In addition, the concentration of **1Fe(IV)=O** may be somewhat overestimated in the UV-vis spectra because of the presence of some other species that absorb at the same wavelength. Finally, after **1Fe(IV)=O** was consumed, no more O_2 was formed. These experimental observations suggest that **1Fe(IV)=O** is the catalyst resting state, and that the addition of Ce(IV) may generate oxo-iron species with a higher oxidation state than IV, and these are directly responsible for the water-oxidation event. Eventually, the **1Fe(IV)=O** was consumed after several catalytic cycles. Taking into consideration the highly oxidant and acidic conditions of the catalytic reactions, catalyst decomposition probably involves ligand oxidation, hydrolysis of the metal complex or both. Further studies to clarify this are underway.

To obtain further insights into the mechanism, we monitored simultaneously the evolution of oxygen (using a pressure transducer) and the consumption of Ce(IV) (using UV-vis spectroscopy). The kinetic study was performed in the 2 mM > [**1Fe**] > 0.075 mM range at pH = 1.0 (kinetic study details are given in Supplementary Section S2.5). First of all, the simultaneous oxygen evolution/cerium consumption indicates that the O_2 formed per CAN consumption corresponded approximately to the expected stoichiometric ratio (1:4) in all the kinetic experiments (see Supplementary Fig. S11 and Table S3). The initial reaction rates for Ce(IV) consumed agree with a first-order process in [**1Fe(IV)=O**] (see Supplementary Figs S12–S15). Identical reaction rates were measured in D_2O and revealed a lack of solvent isotope effect (see Supplementary Table S3). Although the order in Ce(IV) was 0.83 at low Ce(IV) concentrations (5–20 mM), at higher concentrations (25–80 mM) the order decreased to zero (see Supplementary Figs S16–S20). Therefore, the rate-determining step (RDS) at low Ce(IV) concentrations could be viewed as a bimolecular **1Fe(IV)=O**/Ce(IV) reaction, which excludes possible bimetallic iron pathways. The change of the initial rate order at high Ce(IV) concentrations could be attributed to the formation of a reversible **1Fe(IV)=O**/Ce(IV) interaction before the RDS. In this regard, a Lewis acid interaction between Sc^{3+} and the oxo-iron(IV) unit in $[Fe(IV)(O)(tmc))]^{2+}$ (tmc = tetramethylcyclam) was documented recently[26,27].

On the basis of all the experimental evidence, we propose that iron complexes of general formula $[Fe(X)_2(L^{N4})]$ share a common catalytic cycle (Fig. 4). Spectroscopic monitoring demonstrates that the initial Fe(II) complexes $[Fe(X)_2(L^{N4})]$ are oxidized immediately by the excess of Ce(IV) to yield the resting-state water–oxo compound $[Fe(IV)(O)(H_2O)(L^{N4})]^{2+}$, L^{N4}**Fe(IV)=O**. The bimolecular rate law extracted from the kinetic analysis suggests that the RDS involves further $1e^-$ oxidation of the oxo-iron(IV) complex by Ce(IV), to form a highly oxidizing $[Fe(V)(O)(OH_2)(L^{N4})]^{3+}$ intermediate. Given the high oxidation state of the metal centre, the water ligand must be very acidic and the $[Fe(V)(O)(OH)(L^{N4})]^{2+}$ intermediate L^{N4}**Fe(V)=O** is expected to be formed. Subsequent attack of a water molecule, assisted by a hydrogen-bond interaction with the hydroxide ligand, forms the O–O bond, which reduces the iron(V) to form the $[Fe(III)(OOH)(H_2O)(L^{N4})]^{2+}$ intermediate L^{N4}**Fe(III)–OOH**.

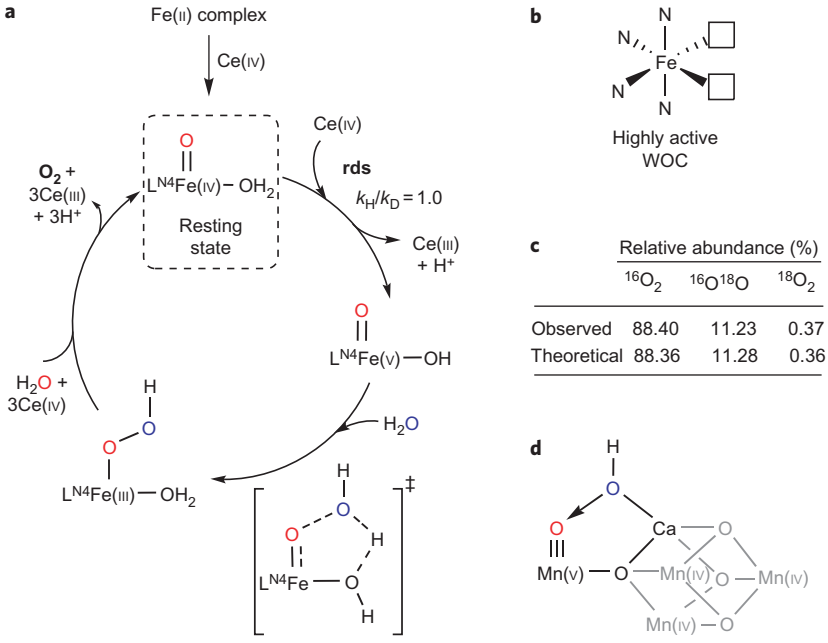

Figure 4 | Postulated mechanism for water oxidation by iron complexes based on tetradentate nitrogen ligands. a, In the catalytic cycle the only intermediate observed was complex **1Fe(IV)=O**, which constituted the resting state. All the other intermediates are postulated. **b**, Iron complexes containing neutral tetradentate nitrogen ligands that provide two *cis* labile coordination sites gave highly active WOCs. **c**, Oxygen isotopic distribution of O_2 obtained with catalyst **1Fe** under typical reaction conditions in a water solution that contained 6% of $H_2^{18}O$. **d**, One proposed mechanism for the O–O bond formation at the $CaMn_4$ cluster in the natural PSII (ref. 36).

The closure of the catalytic cycle can be envisioned as two possible pathways. The first possibility comprises further oxidation of intermediate $\mathbf{L^{N4}Fe(III)–OOH}$ to give $\mathbf{L^{N4}Fe(IV)–OOH}$ or $\mathbf{L^{N4}Fe(V)–OOH}$, and O_2 extrusion via reduction of the metal centre to Fe(II) or Fe(III), respectively. This mechanism finds precedent in the water oxidation at mononuclear ruthenium complexes[28]. Redox potential ($E_{1/2}$) values for Fe(IV)/Fe(III) couples in complexes with N-rich ligands are in the range 0.39 to 0.79 V versus a saturated calomel electrode[29–31], and therefore oxidation by Ce(IV) is envisioned as a thermodynamically favourable process. Indeed, **1Fe(IV)=O** is formed rapidly by reaction of **1Fe** with CAN. In addition, $[Fe(IV)(OOtBu)(OH)(mcp)]^{2+}$ species have been prepared by the oxidation of $[Fe(III)(OOtBu)(mcp)]^{2+}$ with HOOtBu (ref. 32).

The second possibility involves protonation of the hydroperoxide ligand in $\mathbf{L^{N4}Fe(III)–OOH}$ extruding H_2O_2 and forming a Fe(III) species that is oxidized rapidly by Ce(IV), and thus closes the catalytic cycle. Fast and quantitative H_2O_2 oxidation to give O_2 by Ce(IV) was demonstrated indirectly by measurement of the stoichiometric amount of O_2 formed after adding H_2O_2 to a typical reaction mixture with 125 mM CAN. This scenario needs to take into account that $2e^-$ oxidation of H_2O to form H_2O_2 at low pH values has a high $E_{1/2}$ and, *a priori*, oxidation by CAN is slightly thermodynamically unfavourable ($\Delta E_{1/2} = -0.15$). However, coupling this reaction with fast H_2O_2 oxidation by CAN may drive the overall process. In addition, redox potentials are referred to stoichiometric amounts of oxidizing and reducing species, and in the presence of a large excess of CAN the actual potential of the oxidant may be substantially higher.

Concerning the crucial O–O bond-formation reaction, we favour this scheme over other plausible interpretations because the microscopic reverse reaction, which involves the heterolytic cleavage of the O–O bond in $\mathbf{L^{N4}Fe(III)–OOH}$ species to form $\mathbf{L^{N4}Fe(V)=O}$, has been described in catalytic alkane and alkene oxidations mediated by $[Fe(X)_2(L^{N4})]$ complexes[33–35]. Previous density functional theory calculations on the transformation of $\mathbf{L^{N4}Fe(III)–OOH}$ into $\mathbf{L^{N4}Fe(V)=O}$ and H_2O (L = tpa, mep and ^{Me2}Pytacn) computed surmountable activation barriers for O–O lysis/formation reactions, with only a slight thermodynamic preference for the high oxidation state. However, under the highly acidic (pH ~ 1) conditions for water-oxidation reactions, overstabilization of the lower oxidation states must translate into thermodynamic favouring of the reverse O–O bond-forming reaction.

We notice that the suggested transition state for the O–O bond lysis formation is comparable with one of the mechanisms proposed for the O–O bond formation at the $CaMn_4$ cluster in the natural PSII (ref. 36).

In summary, the highly water-soluble catalytic systems presented in this work are based on abundant, environmentally benign iron-based coordination complexes. As far as we know, activities (TON) exhibited by these catalysts constitute the highest values per atom for any first-row transition metal system under homogeneous conditions reported to date, and approach those of the most active Ru- and Ir-based systems. Ligand availability, modularity and versatility of such of coordination complexes are open to the systematic study of a large number of structures. This must allow pinpointing key structural and electronic features of the iron complexes that sustain efficient water oxidation, and eventually will lead to superior catalysts. Already, the present study has allowed us to establish that the presence of two *cis* free coordination sites is a structural key aspect for catalysis. Furthermore, we envision that this motive could represent a general key structural aspect useful in the conceptual design of iron-based homogeneous and heterogeneous WOCs. The highly modular characteristics of the system also suggest that it will be suitable for catalyst heterogenization on solid supports (that is, SiO_2, zeolites, metal–organic frameworks, etc.). Studies aimed at coupling the present systems with photochemical and electrochemical oxidation, as well as detailed studies on the mechanism, are in progress. Iron-based catalysts described herein clearly fill a gap in the design of water-splitting systems, which could eventually enable sustainable artificial photosynthetic schemes.

Methods

Materials. Reagents and solvents were purchased from commercial sources and used as received, unless otherwise stated. CAN ($[[Ce(IV)(NO_3)_6](NH_4)_2]$) ≥98% purity and ≥99.99% purity on a trace-metals basis and $NaIO_4$ ≥ 99.8% purity were purchased from Sigma-Aldrich and used without further purification. $H_2{}^{18}O$ (98% ^{18}O-enriched) was acquired from ICON Services (Summit, New Jersey). Solvents were purchased from SDS and Scharlab. Solvents were purified and dried by passing through an activated alumina purification system (MBraun SPS-800) and stored in an anaerobic glovebox. Preparations of **1Fe** (ref. 23), **1Mn** (ref. 37), **2OTf** (ref. 38), **2Cl** (ref. 38), **3** (ref. 39), **4** (ref. 40), **5** (ref. 41), **6** (ref. 42) and **7** (ref. 43) were carried out as described previously. Water (18.2 MΩ·cm) was purified with a Milli-Q Millipore Gradient AIS system. Further details of the materials are given in the Supplementary Information.

Physical methods. ESI-MS experiments were performed on a Bruker Daltonics Esquire 3000 Spectrometer by introducing samples directly into the ESI source using a syringe pump. GC-MS spectral analyses of isotopic labelled O_2 were performed on an Agilent Series 7890A model G3440A GC chromatograph interfaced with an Agilent Series 5975C MS model G3245A mass spectrometer. UV-vis near infrared spectra were recorded on an Agilent 8453 diode array spectrophotometer (190–1,100 nm range) in 1 cm quartz cells. The temperature control was performed with a cryostat from Unisoku Scientific Instruments, Japan. DLS experiments were performed on a Zetasizer Nano ZS, Malvern Instruments (particle-size distribution from 0.6 to 6,000 nm). NTA experiments were carried out on a NL20 NanoSight (particle concentration measurement 10–2,000 nm). DLS and NTA were carried out at the analysis laboratories of the Institut de Ciència de Materials de Barcelona. Further details of the physical methods are given in the Supplementary Information.

Gas-evolution parallel catalytic studies. A typical run of eight experiments was conducted as follows. All water-oxidation reactions were performed in a 15 ml vial capped with septa and equipped with stir bars. The reactions were performed under an air atmosphere. Negligible differences were obtained when reactions were performed under N_2 or Ar. Each of the eight volume-calibrated vials that contained the oxidant–water solution (that is, 125 mM, 9.5 ml) were connected to one port of a differential pressure transducer sensor (Honeywell-ASCX15DN, ±15 psi). Each reaction had its reference reaction, which was connected to the other port of the differential pressure transducer sensor. The reaction and reference vials were kept under the same experimental conditions to reduce the system noise because of temperature and pressure fluctuations. Subsequently, the reactions were initiated by adding catalyst solutions in Milli-Q water (250 μM, 0.5 ml) via a syringe through septa (typically the final solution had a molarity of 12.5 μM and a final volume of 10 ml, headspace 7.30±0.05 ml). The oxygen evolution of the reactions was monitored by recording the headspace pressure increase (one second intervals). The pressure increase resulted from the difference in pressure between the reaction and reference vials. After the oxygen evolution reached a plateau, the amount of the formed gas was captured and measured by equilibrating the pressure between the reaction and reference vials. The oxygen contained in each of the reaction vials was measured by analysing an aliquot of gas captured at the headspace (0.1 ml) by GC. GC measurements of O_2 corroborated the values obtained by pressure increments. Oxygen traces (Supplementary Figs S6–S10) show single-run reactions, although the final TON and TOF values given in Table 1 and the Supplementary tables were calculated from at least an average of three runs. Further details are given in the Supplementary Information.

Identification and quantification of gases by GC. Oxygen concentrations at the headspace were analysed with an Agilent 7820A GC System equipped with columns, washed molecular sieve 5A, 2 m × 1/8 inch outside diameter (OD), Mesh 60/80 SS and Porapak Q, 4 m × 1/8 inch OD, Mesh 80/100 SS, and a thermal conductivity detector. The O_2 amount obtained was calculated by the difference between air and O_2, and the reaction measured. O_2/N_2 calibration was performed using previously prepared different O_2/N_2 mixtures. Further details are given in the Supplementary Information.

Received 6 June 2011; accepted 2 August 2011; published online 4 September 2011

References

1. US Energy Information Administration. *International Energy Outlook* DOE/EIA-0484 (Office of Integrated Analysis and Forecasting, US Department of Energy).
2. Hoffert, M. I. *et al.* Energy implications of future stabilization of atmospheric CO_2 content. *Nature* **395,** 881–884 (1998).
3. Lewis, N. S. *Energy and Transportation* 33–39 (The National Academies Press, 2003).
4. Ciamician, G. The photochemistry of the future. *Science* **36,** 385–394 (1912).
5. Turner, J. A. Sustainable hydrogen production. *Science* **305,** 972–974 (2004).
6. Dempsey, J. L. *et al.* Molecular chemistry of consequence to renewable energy. *Inorg. Chem.* **44,** 6879–6892 (2005).
7. Yano, J. *et al.* Where water is oxidized to dioxygen: structure of the photosynthetic Mn_4Ca cluster. *Science* **314,** 821–825 (2006).
8. Chen, X., Shen, S., Guo, L. & Mao, S. S. Semiconductor-based photocatalytic hydrogen generation. *Chem. Rev.* **110,** 6503–6570 (2010).
9. Magnuson A. *et al.* Biomimetic and microbial approaches to solar fuel generation. *Acc. Chem. Res.* **42,** 1899–1909 (2009).
10. Tong, L., Duan, L., Xu, Y., Privalov, T. & Sun, L. Structural modifications of mononuclear ruthenium complexes: a combined experimental and theoretical study on the kinetics of ruthenium-catalyzed water oxidation. *Angew. Chem. Int. Ed.* **50,** 445–449 (2011).
11. McDaniel, N. D., Coughlin, F. J., Tinker, L. L. & Bernhard, S. Cyclometalated iridium(III) aquo complexes: efficient and tunable catalysts for the homogeneous oxidation of water. *J. Am. Chem. Soc.* **130,** 210–217 (2008).
12. Hull, J. F. *et al.* Highly active and robust Cp* iridium complexes for catalytic water oxidation. *J. Am. Chem. Soc.* **131,** 8730–8731 (2009).
13. Lalrempuia, R., McDaniel, N. D., Müller-Bunz, H., Bernhard, S. & Albrecht, M. Water oxidation catalyzed by strong carbene-type donor–ligand complexes of iridium. *Angew. Chem. Int. Ed.* **49,** 9765–9768 (2010).
14. Enthaler, S., Junge, K. & Beller, M. Sustainable metal catalysis with iron: from rust to a rising star? *Angew. Chem. Int. Ed.* **47,** 3317–3321 (2008).
15. Ruettinger, W. F., Campana, C. & Dismukes, G. C. Synthesis and characterization of $Mn_4O_4L_6$ complexes with cubane-like core structure: a new class of models of the active site of the photosynthetic water oxidase. *J. Am. Chem. Soc.* **119,** 6670–6671 (1997).
16. Brimblecombe, R., Swiegers, G. F., Dismukes, G. C. & Spiccia, L. Sustained water oxidation photocatalysis by a bioinspired manganese cluster. *Angew. Chem. Int. Ed.* **47,** 7335–7338 (2008).
17. Dismukes, G. C. *et al.* Development of bioinspired Mn_4O_4-cubane water oxidation catalysts: lessons from photosynthesis. *Acc. Chem. Res.* **42,** 1935–1943 (2009).
18. Limburg, J. *et al.* A functional model for O–O bond formation by the O_2-evolving complex in photosystem II. *Science* **283,** 1524–1527 (1999).
19. Kanan, M. W. & Nocera, D. G. *In situ* formation of an oxygen-evolving catalyst in neutral water containing phosphate and Co^{2+}. *Science* **321,** 1072–1075 (2008).
20. Yin, Q. *et al.* A fast soluble carbon-free molecular water oxidation catalyst based on abundant metals. *Science* **328,** 342–345 (2010).
21. Huang, Z. *et al.* Efficient light-driven carbon-free cobalt-based molecular catalyst for water oxidation. *J. Am. Chem. Soc.* **133,** 2068–2071 (2011).
22. Ellis, W. C., McDaniel, N. D., Bernhard, S. & Collins, T. J. Fast water oxidation using iron. *J. Am. Chem. Soc.* **132,** 10990–10991 (2010).
23. Company, A. *et al.* Alkane hydroxylation by a nonheme iron catalyst that challenges the heme paradigm for oxygenase action. *J. Am. Chem. Soc.* **129,** 15766–15767 (2007).
24. Company, A. *et al.* Modeling the *cis*-oxo-labile binding site motif of non-heme iron oxygenases: water exchange and oxidation reactivity of a non-heme iron(IV)–oxo compound bearing a tripodal tetradentate ligand. *Chem. Eur. J.* **17,** 1622–1634 (2011).
25. Garcia-Bosch, I. *et al.* Evidence for a precursor complex in C–H hydrogen atom transfer reactions mediated by a manganese(IV)–oxo complex. *Angew. Chem. Int. Ed.* **50,** 5648–5653 (2011).
26. Fukuzumi, S. *et al.* Crystal structure of a metal ion-bound oxoiron(IV) complex and implications for biological electron transfer. *Nature Chem.* **2,** 756–759 (2010).
27. Morimoto, Y. *et al.* Metal ion-coupled electron transfer of a nonheme oxoiron(IV) complex: remarkable enhancement of electron-transfer rates by Sc^{3+}. *J. Am. Chem. Soc.* **133,** 403–405 (2011).
28. Chen, Z. *et al.* Nonaqueous catalytic water oxidation. *J. Am. Chem. Soc.* **135,** 17670–17673 (2010).
29. Fukuzumi, S., Kotani, H., Lee, Y-M. & Nam, W. Sequential electron-transfer and proton-transfer pathways in hydride-transfer reactions from dihydronicotinamide adenine dinucleotide analogues to non-heme oxoiron(IV) complexes and *p*-chloranil. Detection of radical cations of NADH analogues in acid-promoted hydride-transfer reactions. *J. Am. Chem. Soc.* **130,** 15134–15142 (2008).
30. Comba, P., Fukuzumi, S., Kotani, H. & Wunderlich, S. Electron-transfer properties of an efficient nonheme iron oxidation catalyst with a tetradentate bispidine ligand. *Angew. Chem. Int. Ed.* **49,** 2622–2625 (2010).
31. Wang, D., Zhang, M., Bühlmann, P. & Que, L. Jr Redox potential and C–H bond cleaving properties of a nonheme Fe(IV)=O complex in aqueous solution. *J. Am. Chem. Soc.* **132,** 7638–7644 (2010).
32. Jensen, M. P. *et al.* High-valent nonheme iron. Two distinct iron(IV) species derived from a common iron(II) precursor. *J. Am. Chem. Soc.* **127,** 10512–10525 (2005).
33. Company, A. *et al.* Olefin-dependent discrimination between two nonheme HOFe(V)=O tautomeric species in catalytic H_2O_2 epoxidations. *Chem. Eur. J.* **15,** 3359–3362 (2009).
34. Bassan, A., Blomberg, M. R. A., Siegbahn, P. E. M. & Que, L. Jr A density functional study of O–O bond cleavage for a biomimetic non-heme iron complex demonstrating an Fe^V-intermediate. *J. Am. Chem. Soc.* **124,** 11056–11063 (2002).
35. Quinonero, D., Morokuma, K., Musaev, D. G., Mas-Balleste, R. & Que, L. Jr Metal–peroxo versus metal–oxo oxidants in non-heme iron-catalyzed olefin oxidations: computational and experimental studies on the effect of water. *J. Am. Chem. Soc.* **127,** 6548–6549 (2005).

36. Dau, H. *et al.* The mechanism of water oxidation: from electrolysis via homogeneous to biological catalysis. *ChemCatChem* **2,** 724–761 (2010).
37. Garcia-Bosch, I., Company, A., Fontrodona, X., Ribas, X. & Costas, M. Efficient and selective peracetic acid epoxidation catalyzed by a robust manganese catalyst. *Org. Lett.* **10,** 2095–2098 (2008).
38. Costas, M. & Que, L. Jr Ligand topology tuning of iron-catalyzed hydrocarbon oxidations. *Angew. Chem. Int. Ed.* **41,** 2179–2181 (2002).
39. Suzuki, K., Oldenburg, P. D. & Que L. Jr Iron-catalyzed asymmetric olefin *cis*-dihydroxylation with 97% enantiomeric excess. *Angew. Chem. Int. Ed.* **47,** 1887–1889 (2008).
40. Britovsek, G. J. P., England, J. & White, A. J. P. Non-heme iron(II) complexes containing tripodal tetradentate nitrogen ligands and their application in alkane oxidation catalysis. *Inorg. Chem.* **44,** 8125–8134 (2005).
41. Lim, M. H. *et al.* An Fe^{IV}=O complex of a tetradentate tripodal nonheme ligand. *Proc. Natl Acad. Sci. USA* **100,** 3665–3670 (2003).
42. Nam, W., Ho, R. Y. N. & Valentine, J. S. Iron–cyclam complexes as catalysts for the epoxidation of olefins by 30% aqueous hydrogen peroxide in acetonitrile and methanol. *J. Am. Chem. Soc.* **113,** 7052–7054 (1991).
43. Roelfes, G. *et al.* End-on and side-on peroxo derivatives of non-heme iron complexes with pentadentate ligands: models for putative intermediates in biological iron/dioxygen chemistry. *Inorg. Chem.* **42,** 2639–2653 (2003).

Acknowledgements

We thank R. Hage, X. Ribas and P. Lahuerta for reading this work and for comments. We thank the European Research Foundation for project FP7-PEOPLE-2010-ERG-268445 (J.Ll.), El Ministerio de Ciencia e Innovación for project CTQ2009-08464 (M.C.), for a Ramon y Cajal contract (J.Ll.) and for a PhD grant (I.G-B.), Generalitat de Catalunya for an ICREA Academia Award and the European Research Council for Project ERC-2009-StG-239910 (M.C.). RahuCat is acknowledged for giving the tritosylTACN.

Author contributions

J.Ll. and M.C. devised the initial concept for the work and designed the experiments. Z.C., I.G-B., L.G. and J.Ll. carried out the experiments. J.J.P. and J.Ll. designed the differential pressure transducer hardware and software. Z.C., I.G-B. and J.Ll. analysed the data. J.Ll. and M.C. co-wrote the manuscript.

Additional information

The authors declare no competing financial interests. Supplementary information and chemical compound information accompany this paper at www.nature.com/naturechemistry. Reprints and permission information is available online at http://www.nature.com/reprints. Correspondence and requests for materials should be addressed to J.L.F. and M.C.